Development and Application of a Visible–Infrared Rain Flag for Scatterometer Data

CHRISTOPHER GRASSOTTI, S. MARK LEIDNER, JEAN-FRANÇOIS LOUIS, AND ROSS N. HOFFMAN

Atmospheric and Environmental Research, Inc., Cambridge, Massachusetts

(Manuscript received 6 July 1998, in final form 25 September 1998)

ABSTRACT

The authors report on characteristics of a rain flag derived from collocation of visible and infrared image data with rain rates over the North Atlantic Ocean obtained from microwave imagery (SSM/I) during a 3-week period (15 October 1996–2 November 1996). The rain flag has been developed as part of an effort to provide an indication of contamination by heavy rainfall in NASA scatterometer datasets. The primary results of this analysis indicate 1) that a simple albedo/infrared brightness temperature threshold is capable of flagging most of the heavy rainfall, though with a fairly high rate of false alarms, and 2) that the small difference in optimal threshold between the Tropics and midlatitudes can probably be ignored. Use of the rain flag in 12 assimilation experiments during this period showed that the number of rain-flagged wind vector cells is generally less than 1% of the number of cells. Overall, the impact from using the rain-flagged data is generally less than 5 m s^{-1} and localized (less than 5° of latitude and longitude). However, in some cases, the effect of excluding just one to five rain-flagged points can change the resulting analysis significantly, because their placement is critical for defining the flow along a front or some other shear-dominated environment.

1. Introduction

It is known that measurements of Ku-band (13.4 GHz) backscatter from active microwave scatterometers such as the NASA scatterometer (NSCAT) that operated on board the Advanced Earth Observing Satellite (ADEOS) satellite during its nine-month lifetime can be contaminated by the presence of heavy rainfall in the antenna beam (Guymer et al. 1981; Spencer and Shimada 1991; Smith and Wentz 1998). The effect of rainfall on the backscatter signal is complex: both attenuation and amplification are possible, depending on the rain intensity, viewing angle, and wind speed. Though it may eventually be possible to correct for these effects, our purpose in this investigation is, more modestly, to develop a rain flag that could be used to identify measurements with a high probability of rain contamination. One may then simply eliminate those flagged measurements from subsequent wind analyses.

For NSCAT and its interim successor QuikSCAT (QSCAT), devising a rain flag is made difficult by the absence of an onboard passive microwave instrument that could be used effectively to delineate regions with moderate to heavy rainfall. Because of this, we have chosen to make use of visible (VIS) and infrared (IR) imagery, which is routinely available from the operational suite of geostationary satellites such as GOES and GMS. Data from these platforms are available generally every half-hour to hour for large regions equatorward of approximately 60°N and 60°S. The focus of this article is twofold. First, we report on characteristics of the derived rain flag obtained from a preliminary study using a 3-week dataset consisting of collocated *GOES-8* imagery and Special Sensor Microwave/Imager (SSM/I) derived rain rates. We examined both temporal and spatial characteristics of the VIS–IR flags and the skill of these flags with respect to instantaneous rain-rate categories. Second, we conducted a number of data assimilation experiments during this time period to evaluate the impact of the rain flag on surface wind analyses that used the NSCAT observations.

2. Rain flag determination

a. Data

The data used for this study covering the time period 15 October 1996–2 November 1996 were *GOES-8* imagery over the North Atlantic Ocean, and instantaneous rain rates derived from the multichannel SSM/I onboard the Defense Meteorological Satellite Program (DMSP) *F-10* satellite.

GOES-8 data were remapped to a 0.25° latitude–longitude grid, covering the region 0°–60°N latitude and 270°–330°E longitude. The geostationary imager data used were visible albedos from channel 1 (0.62 μm)

Corresponding author address: Christopher Grassotti, Atmospheric and Environmental Research, Inc., 840 Memorial Drive, Cambridge, MA 02139.
E-mail: cgrass@aer.com

and infrared brightness temperatures from channel 4 (10.7 μm). The albedo data were normalized by the cosine of the solar zenith angle.

SSM/I rain rates produced using the algorithm of Wentz (1992) are available globally over the ocean from Remote Sensing Systems, Inc., already mapped to the same 0.25° grid. This algorithm has been developed and tested over several years and has been validated in a number of algorithm intercomparison campaigns (e.g., the Global Precipitation Climatology Project, and the Precipitation Intercomparison Project). Results from these studies show that it performs comparably to other microwave-based algorithms. Recently, in a detailed review of results from the NASA WetNet Second Precipitation Intercomparison Project (PIP-2), Smith et al. (1998) showed most microwave algorithms to have root-mean-square errors on the order of 1 to perhaps 4 mm h^{-1} and bias uncertainties of $\pm 30\%$ of the true rain rate. A large degree of the uncertainty in microwave accuracy estimates is related to the lack and uncertain quality of ground-based verification data, especially over oceans. Since we are more concerned with using the microwave measurements to flag the degree of attenuation at the NSCAT Ku band, rather than specify a precise rain rate, we believe that the threshold tuning procedure we use here is robust with respect to uncertainties in the SSM/I rain rates.

b. Methodology

The approach we use is based on the intuitive notion that cold (or high) and bright clouds are more likely to be heavy rain producers than warmer and less reflective clouds. This idea has been used by a number of researchers in the past, for example, Barrett and Martin (1981), Arkin (1979), Grassotti and Garand (1994), and Negri and Adler (1987); methods based on visible and infrared data perform comparably to microwave retrievals in obtaining rainfall on monthly and longer timescales. This is partly due to the spatial and temporal sampling limitations of the microwave instruments that are situated aboard polar orbiting satellites. However, for short timescales and instantaneous rain rates, the indirect nature of the VIS and IR measurements leads to larger errors, and significant biases and training data dependencies (Ebert 1995). For the NSCAT data the task is somewhat simpler since we seek to flag only moderate to heavy rain areas, rather than to retrieve the rain rate itself. An obvious limitation associated with the use of visible data is the restriction that the technique may only be employed during daytime. Nevertheless, the capability to add an additional level of quality control for up to one-half the scatterometer observations would be extremely useful.

In this study we used the two channels from *GOES-8* in conjunction with the rain rates from the DMSP SSM/I. The objective is to find the thresholds in the visible and infrared data that best correspond to a rain (greater than a critical value)/no rain determination as seen in the SSM/I data. We find the optimum thresholds by maximizing the Heidke skill score (Doswell et al. 1990). This metric is based on a binary rain/no rain contingency table and is designed for situations in which the phenomenon of interest occurs rarely. The optimum visible and infrared thresholds will depend on the choice of critical rain rate; in this study we explored both 5 and 10 mm h^{-1}.

TABLE 1. Schematic contingency table.

	Observed		
Prediction	Rain	No rain	Total
Rain	x	z	$x + z$
No rain	y	w	$y + w$
Total	$x + y$	$z + w$	N

If we consider a schematic prediction contingency table as shown in Table 1 then the Heidke skill score, HSS, is defined as

$$\mathrm{HSS} = \frac{C - E}{N - E},$$

where C is the correct number of predictions out of the total number N,

$$C = x + w,$$

and E is the correct number of predictions due to chance,

$$E = [(x + z)(x + y) + (z + w)(y + w)]/N.$$

The HSS can vary in the range from -1 to $+1$ but more generally lies in the range 0 to 1, with 1 representing perfect skill and 0 the skill of a random prediction.

We can also define the probability of detection, POD, as

$$\mathrm{POD} = x/(x + y)$$

and the false alarm ratio, FAR, which is given as

$$\mathrm{FAR} = z/(x + z).$$

In essence, the POD represents the fraction of all raining points that were correctly identified, while the FAR indicates the percentage of all rain-flagged points which were, in fact, not raining. Ideally, one would like to maximize the POD, while not producing a large FAR.

From the basic contingency sums, x, y, z, and w, all these metrics may be calculated. We computed the sums and corresponding metrics for individual 1-week periods within the entire 19-day period. We also stratified the sums by latitude band into midlatitude (30°–60°N), and tropical (0°–30°N). These are presented in the following section.

c. Results

Figure 1 contains results obtained from data acquired during the first week of the study (15–21 October 1996),

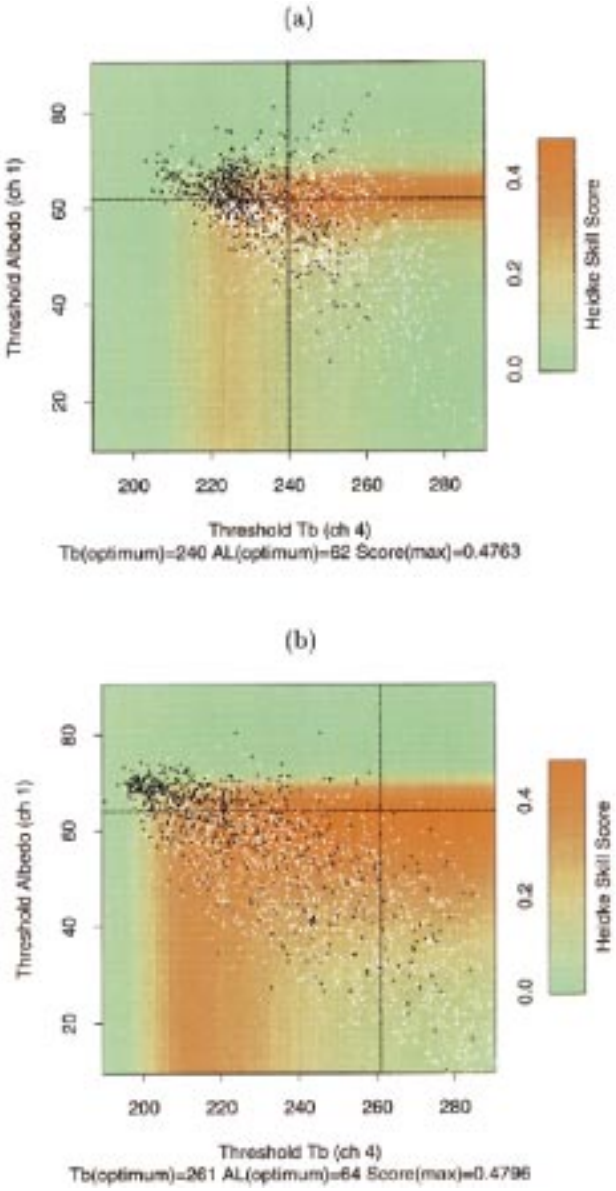

FIG. 1. Heidke skill score optimization for critical rain rate of 5 mm h^{-1} during the period 15–21 October 1996. Score is calculated for various thresholds of IR brightness temperature and VIS albedo. Results are shown for (a) midlatitudes, and (b) Tropics. Optimum combined thresholds (indicated by dashed lines) are IR temperature of 240 K and albedo of 62% in midlatitudes, and 261 K and albedo of 64% in Tropics.

which is the training period in the midlatitudes and Tropics. Both panels show the values of albedo and blackbody temperature of all the rainy points in the sample, plotted as a scatter diagram. Each point is color coded: black if the SSM/I data indicates a rain rate greater than 5 mm h^{-1}, and white for lighter precipitation. The points with no rain at all are not plotted, for clarity of the diagram, but are included in the HSS computation. The behavior of the Heidke skill score is shown in color in the background of the plots, as a function of the visible and infrared thresholds, which define the predicted rain/no rain boundary. With a sufficiently large number of rain data points in the sample, we expect the skill score to be well behaved. Indeed, both figures show the score to vary smoothly with a maximum value of approximately 0.5. We define the optimum thresholds to be the brightness temperature (TB) and albedo (AL) at which the corresponding HSS is a maximum. For the midlatitude data the optimum TB and AL thresholds that correspond to the critical rain rate of 5 mm h^{-1} are 240 K and 62%, and in the Tropics the corresponding thresholds are 261 K and 64%. They are indicated by the dashed lines in the figures; the point of intersection is the optimum VIS–IR threshold.

Several important features are evident in these figures. First, we see that visible data adds information (skill) pertaining to rainfall in both regions. This is confirmed by the fact that the scores are consistently higher at AL $= 60\%$ for most values of TB than at the bottom edge of the figure (which corresponds to an IR-only rain flag). Also, we can see that for this dataset a VIS-only method is more effective in flagging rain cells than an IR-only method. Second, there is a marked difference in the figures, due to a difference in the joint distribution of AL and TB. In the Tropics, in scenes containing more reflective pixels (AL $\geq 60\%$), there are very few warm pixels. Since most of these bright pixels are also cold, varying the TB threshold from 240 K to 300 K has almost no effect on the score, when the AL threshold is greater than or equal to 60%. The midlatitude distribution of AL and TB differs in that some pixels with AL approximately equal to 60% are also those with TB between 240 K and 270 K. When matched with the SSM/I rain data this means that one sees improved skill for an AL threshold of 62%, when the TB threshold is reduced from 270 K to 240 K. Finally, it is evident from the scatter diagrams that there is no clear separation between light and heavy rain: black and white points overlap to a large extent. That is the reason why the Heidke skill score is not large, even for the optimum threshold. (See additional discussion in following section.)

The optimum VIS–IR thresholds were derived in a similar manner to those above for both critical rain-rate categories (5 and 10 mm h^{-1}), and for each week. These results for both midlatudes and Tropics are contained in Table 2. In all categories, the optimum albedo thresholds are quite stable from week to week, varying by only 1% or 2% within a category. Albedo thresholds in the Tropics seem to be marginally higher than those in the midlatitudes, and also exhibit the expected tendency of being generally higher at 10 than at 5 mm h^{-1}. Optimum TB thresholds are more variable in each category. For example, in the Tropics the thresholds associated with 5 mm h^{-1} decreases by nearly 30 K from the first week to the last. There is no clear trend over the 3-week period, with some categories showing increases, and

TABLE 2. Optimum thresholds as a function of week and critical rain rate. Note that the last week contains five days.

	0°–30°N				30°–60°N			
	RR > 5		RR > 10		RR > 5		RR > 10	
Time period	TB	AL	TB	AL	TB	AL	TB	AL
15 Oct–21 Oct	**261**	**64**	**225**	**66**	**240**	**62**	**228**	**63**
22 Oct–28 Oct	248	65	219	66	249	61	242	62
29 Oct–2 Nov	233	64	232	68	227	61	212	61
All data	276	64	229	66	240	62	230	63

others showing decreases. Part of the variability may be associated with reduced sample sizes in the last period (see the parameter NR in Tables 3 and 4). Like albedo, the optimum TB thresholds vary with rain rate as expected—in this case, however, decreasing with increasing rain rate.

We then applied the optimum thresholds found for the first week of data (boldface in Table 2) on the data in each of the three weeks studied. These results are shown in Tables 3 and 4, which contain the metrics HSS, POD, FAR, and NR (number of raining points). For comparison, the HSS corresponding to the optimum thresholds of that week's data are also included in parentheses, showing the highest score achievable using the threshold approach.

In general, the rain flag performs worse at the end of the study period than during the first week as defined by all three metrics. However, when the rain flag is evaluated relative to its theoretical ''optimum,'' that is comparing the HSS to the value in parentheses, we see that the declining scores are due more to limitations in the two-channel method, than to a problem of retuning.

Additional insight into the nature of the rain-flag errors is provided if we compute the skill scores using ''buffers'' of ± 1 mm h^{-1} and ± 2 mm h^{-1} for the rain/no rain determination (Table 5). For example, in the case of a 1 mm h^{-1} buffer, a point where the AL/TB threshold method predicts 5 mm h^{-1} or more is considered correct if the SSM/I data shows more than 4 mm h^{-1}. Conversely, a no-rain prediction is considered correct if the SSM/I data shows less than 6 mm h^{-1} of rain. This has the effect of moving elements onto the main diagonal in the contingency table (see Table 1). If many of the classification errors are occurring for events when the observed rain rate is close to the critical threshold (this range of rain rates defined by the buffer size), then such an adjustment will have a marked positive effect on the skill scores. Results from Table 5 show that all scores are noticeably improved. For instance, during the first week the HSS increases from 0.48 to 0.64. This indicates that many of the misclassifications are subtle.

In many applications, such as the one presented below, it is important to eliminate the points that are contaminated by heavy rain, but it is less important to retain all the uncontaminated points because the data density is very high. Figure 2 shows that, despite a relatively low HSS, the threshold method is able to detect almost 100% of the points with very high precipitation, with a low rate of false alarms for light precipitation.

d. Rain flag examples

Figures 3 and 4 show two examples of the rain flag corresponding to specific scenes using a critical rain rate of 5 mm h^{-1}. The first, from 19 October 1996, shows the case of Hurricane Lili as it moved north through the western Atlantic Ocean. The figure panels contain the visible and infrared *GOES-8* imagery, the observed SSM/I rain rates, and the rain-flag results; the latter has been coded by colors that correspond to each element of the rain/no rain contingency table. In general, the rain flag performs quite reasonably, detecting much of the rain area associated with the hurricane, and also that connected with a prolonged heavy rain event over the U.S. east coast. The second case, valid on 25 October 1996, shows the SSM/I observations and rain flag results over the northern Atlantic Ocean. Again, the flag successfully detects much of the rain, although the amount of false alarms and undetected events is also higher.

TABLE 3. Rain-flag verification scores in the region 30°–60°N as a function of week and critical rain rate. See text for variable definitions. Scores are based on using optimum AL and TB thresholds found from dependent data (15 Oct–21 Oct). The HSS corresponding to the optimum thresholds of that week's (dependent) data are also included in parentheses.

	30°–60°N							
	RR > 5 mm h^{-1}				RR > 10 mm h^{-1}			
Time period	NR	HSS	POD	FAR	NR	HSS	POD	FAR
15 Oct–21 Oct	651	0.48 (0.48)	0.53	0.56	282	0.45 (0.45)	0.51	0.59
22 Oct–28 Oct	542	0.32 (0.34)	0.30	0.64	207	0.13 (0.25)	0.12	0.85
29 Oct–2 Nov	317	0.29 (0.35)	0.47	0.78	113	0.25 (0.36)	0.48	0.83

TABLE 4. Rain-flag verification scores in the region 0°–30°N as a function of week and critical rain rate. See Table 3 for details.

	0°–30°N							
	RR > 5 mm h^{-1}				RR > 10 mm h^{-1}			
Time period	NR	HSS	POD	FAR	NR	HSS	POD	FAR
15 Oct–21 Oct	700	0.48 (0.48)	0.50	0.53	266	0.41 (0.41)	0.57	0.68
22 Oct–28 Oct	673	0.51 (0.52)	0.60	0.54	256	0.41 (0.42)	0.66	0.70
29 Oct–2 Nov	259	0.43 (0.44)	0.49	0.61	60	0.21 (0.26)	0.47	0.86

3. Rain flag application to NSCAT data

a. Approach

To assess the impact of rain on the quality of scatterometer-derived winds, we compare surface wind analyses created with and without rain-flagged data. One characteristic of the scatterometer observations is that the backscatter measurements are consistent with up to four wind vectors. These possible solutions are known as ambiguities. Much effort has gone into devising methods for choosing the ''correct'' solution, but some form of additional a priori information is generally required. In this work, a variational approach is used to combine ambiguous scatterometer winds with a background estimate of the wind field. Finding an analysis that is the best fit to the NSCAT data alone could produce an unrealistic wind field, and so we require that the analysis also satisfy constraints that ensure smoothness and dynamical consistency in the wind field. The best fit to the NSCAT data and other constraints determines the optimal analysis. A complete discussion of our variational method is contained in Hoffman (1984).

Twelve analysis times were chosen during the 3-week period of this study. The analyses were created on a 1° resolution grid over the North Atlantic; 0°–60°N latitude and 270°E–360° (90°W–0°) longitude. ECMWF analyses at 1200 UTC are used as the background or first-guess fields and all available NSCAT data within 3 h of the analysis time are selected.

To accommodate rain flagging, *GOES-8* IR brightness temperature and albedo were first collocated with NSCAT wind vector cells (WVC) and appended to level 2.0 NSCAT HDF files as new scientific datasets. These NSCAT wind vectors were retrieved at 50-km resolution using the NSCAT1 model function. *GOES-8* and NSCAT data are collocated to within 30 min and 0.25° latitude and longitude. Most collocations are within 15 min since we generally have GOES data every 30 min. Including *GOES-8* data in the HDF data file allows for the use of any threshold values of IR brightness temperature and albedo to flag raining areas. For cases presented here, the optimum midlatitude threshold values for a critical rain rate of 5 mm h^{-1} are used (TB < 240 K, AL > 62%). (Threshold values could, and perhaps should, vary in space and time, though not enough training data are presently available to specify this kind of variation.)

Table 6 shows the number of NSCAT WVCs flagged for rain in these 12 cases. A small percentage (0.5%–2%) of WVCs are flagged in each case. In most cases, flagged WVCs occur in groups and coincide with bright, cold clouds associated with synoptic fronts or tropical convection. Figure 5 shows a typical cluster of rain-flagged points along a synoptic front in the middle North Atlantic. Excluding data suspected of rain contamination has a small impact on the analyses. Vector wind speed differences between analyses using rain-flagged data and analyses excluding rain-flagged data for the 12 cases are 0.2–6 m s^{-1} and occur in the immediate vi-

TABLE 5. Rain-flag verification scores in the region 30°–60°N as a function of week for a critical rain rate of 5 ± 1 mm h^{-1}. Scores are based on using optimum AL and TB thresholds found from dependent data (15 Oct–21 Oct). Improved scores with respect to those in Table 3 indicate many rain-flag errors are for rain rates close to the critical rain rate.

	30°–60°N					
	RR > 5 ± 1 mm h^{-1}			RR > 5 ± 2 mm h^{-1}		
Time period	HSS	POD	FAR	HSS	POD	FAR
15 Oct–21 Oct	0.55	0.63	0.50	0.64	0.73	0.41
22 Oct–28 Oct	0.40	0.40	0.60	0.49	0.50	0.51
29 Oct–2 Nov	0.40	0.63	0.70	0.49	0.75	0.63

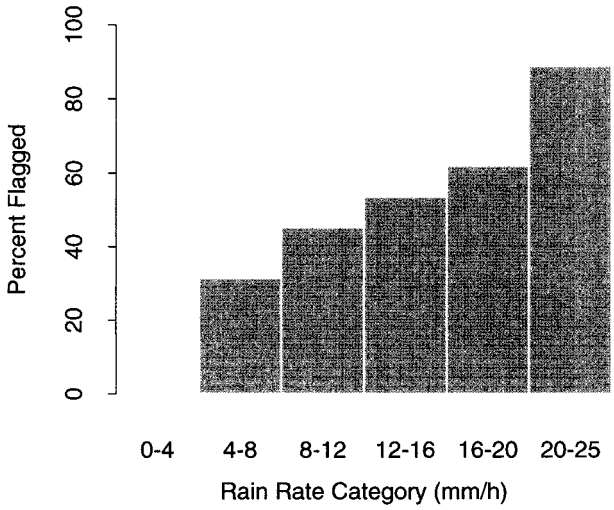

FIG. 2. Percentage of points rain flagged as a function of rain-rate category for midlatitudes for period 15–21 October 1996. IR temperature and albedo thresholds used corresponded to a critical rain rate of 5 mm h^{-1}.

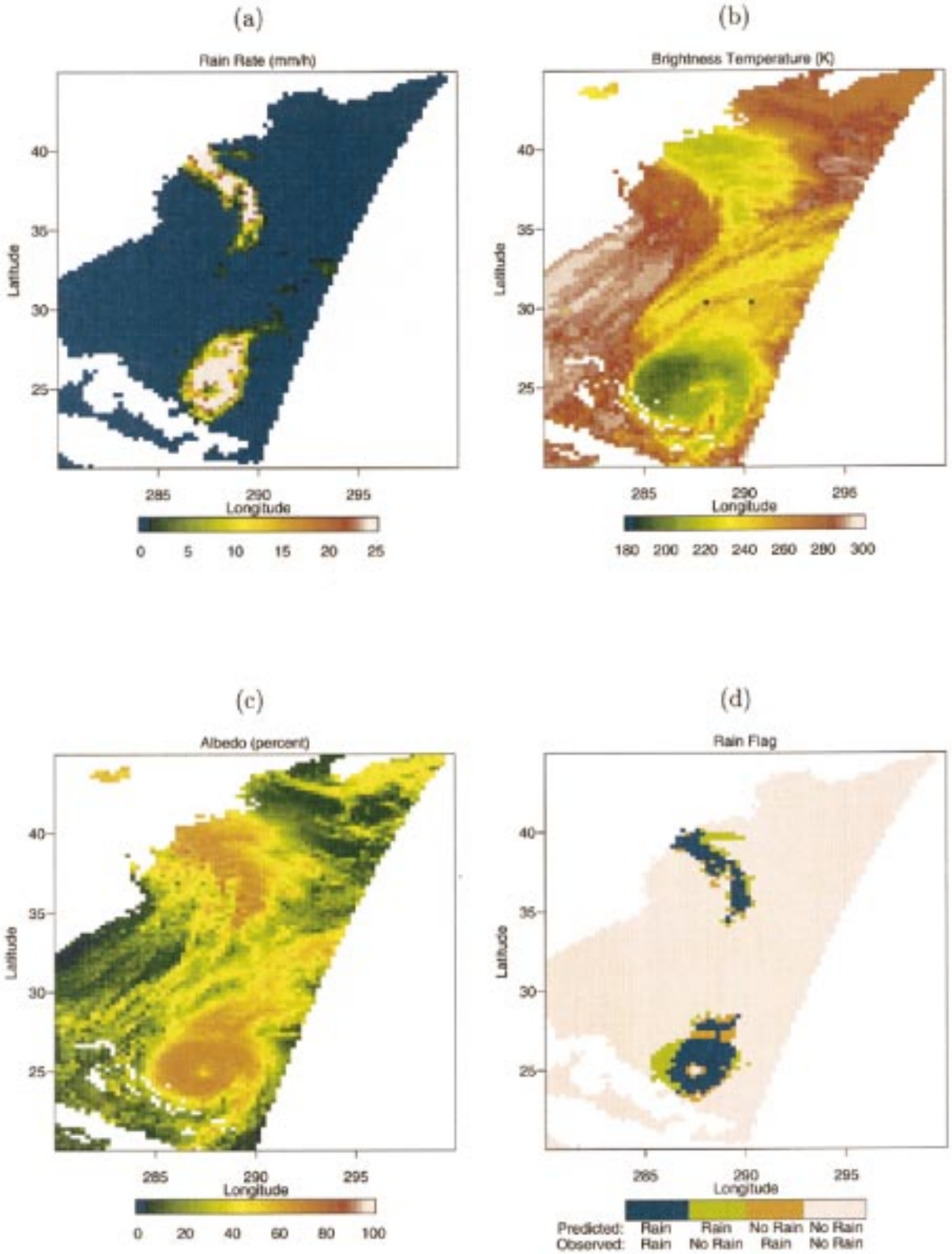

FIG. 3. Case of Hurricane Lili (19 October 1996). (a) SSM/I rain rates (mm h^{-1}), (b) infrared channel brightness temperatures (K), (c) visible channel albedo (percent), and (d) rain-flag results (blue: correctly flagged rain; green: incorrectly flagged rain/false alarm; brown: undetected rain; pink: correctly detected nonrain). In all panels, horizontal and vertical axis units are degrees east longitude and latitude, respectively.

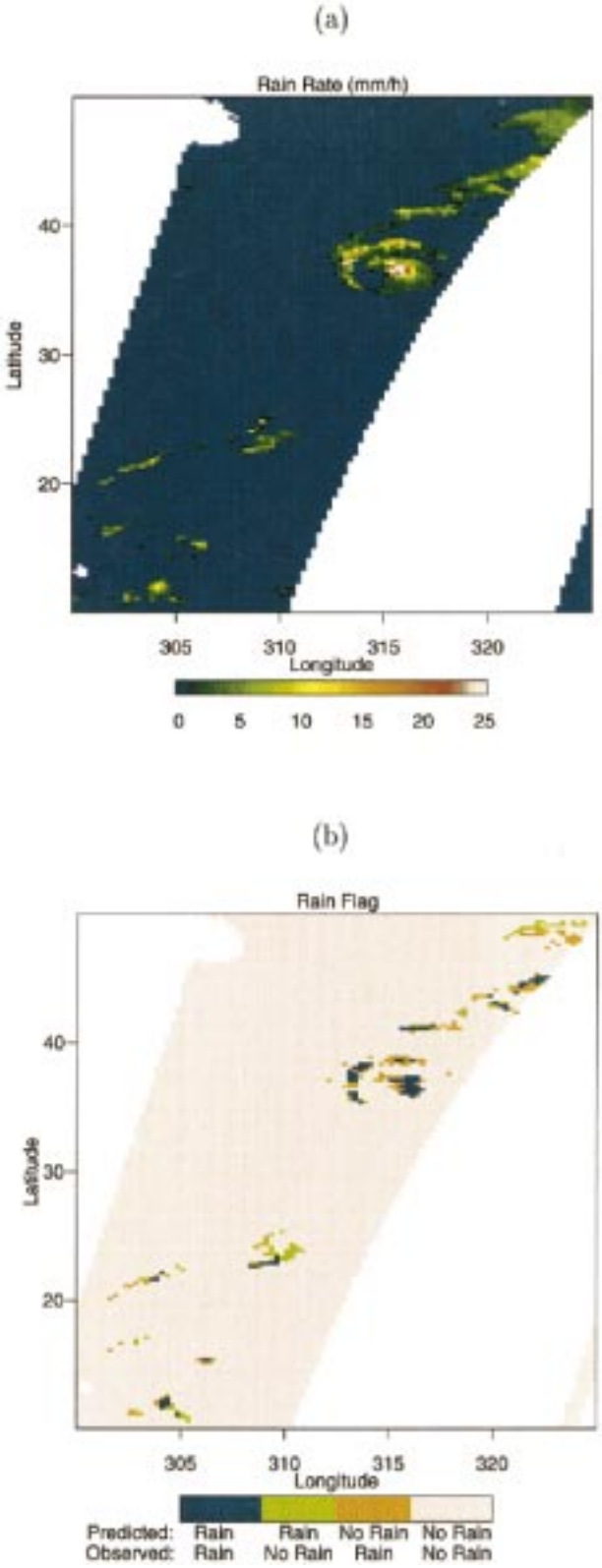

FIG. 4. Case of 25 Oct 1996. Panels are (a) SSM/I rain rates (mm h^{-1}), and (b) rain-flag results (blue: correctly flagged rain; green: incorrectly flagged rain/false alarm; brown: undetected rain; pink: correctly detected nonrain). In all panels, horizontal and vertical axis units are degrees east longitude and latitude, respectively.

TABLE 6. Summary of NSCAT data flagged for rain.

Date	No. WVCs	No. Flagged	% Flagged
15 Oct 1996	4100	59	1.4
16 Oct 1996	3065	58	1.9
17 Oct 1996	2797	10	0.4
18 Oct 1996	2749	35	1.3
19 Oct 1996	3971	19	0.5
26 Oct 1996	2513	32	1.3
27 Oct 1996	2837	34	1.2
28 Oct 1996	2152	39	1.8
30 Oct 1996	4075	68	1.7
31 Oct 1996	3008	57	1.9
01 Nov 1996	2780	12	0.4
02 Nov 1996	3081	25	0.8

cinity (2–3 degrees of latitude and longitude) of the excluded data.

b. Results

Two cases are presented here to illustrate the effects of withholding flagged scatterometer winds on surface wind analyses. These cases demonstrate moderate to high impact on the analyzed wind field compared to the other 10 cases.

1) SYNOPTIC FRONT

The scatterometer passed over part of a synoptic cold front in the middle North Atlantic (30°N, 45°W) at 1417 UTC 16 October 1996. Figure 6a shows analyses using rain-flagged data (black barbs) and excluding rain-flagged data (red barbs). Away from the front, where no data are flagged, the two analyses are essentially identical. In the vicinity of the front, the analyses differ by up to 4 m s^{-1} (vector wind difference). Excluding raining points along the front changes both wind speed and direction. The transition from northwest flow behind the front to southwest flow parallel to the front is smoother, both in speed and direction, in the analysis that excludes flagged data.

Beneath suspected raining points, analyzed wind speeds are reduced by 1–2 m s^{-1} when flagged data are excluded. Figure 6b shows a close-up of NSCAT ambiguous winds in the vicinity of the front. The excluded data have higher wind speeds than either surrounding scatterometer winds or the background analysis (not shown). Note that ambiguous wind speeds ahead and behind the front are $\leq$7 m s^{-1}, while in suspected raining areas, ambiguous wind speeds are roughly doubled (7–15 m s^{-1}). The wind directions for a number of the excluded data are also in disagreement with surrounding scatterometer winds and the background analysis. Southerly winds can be seen in the ambiguous winds in Fig. 6b that do not agree with the southwesterly winds elsewhere in the scatterometer data and background analysis. When these data are included, the analyzed winds back to the south and the wind shift is more abrupt.

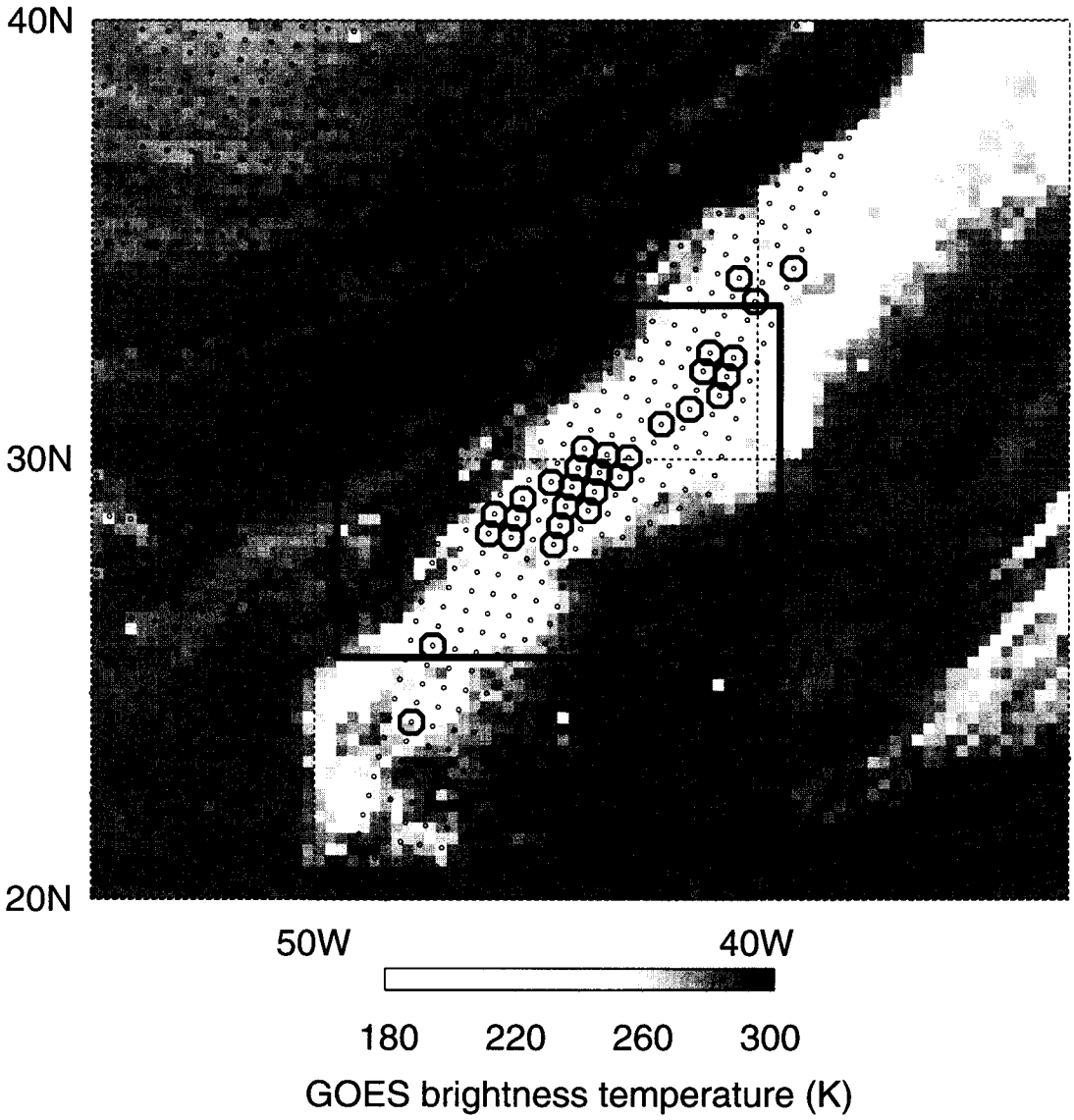

FIG. 5. GOES IR brightness temperature (K) 1415 UTC 16 Oct 1996. NSCAT WVC locations are marked by fine black circles, and WVCs flagged for rain (>5 mm h^{-1}) are circled.

Similar results were found along synoptic fronts in two other cases: 15 October and 31 October 1996 (not shown).

2) TROPICAL CONVECTION

The scatterometer measured winds at the edge of a convective region in the tropical Atlantic (9°N, 48°W) at 1424 UTC 27 October 1996. As commonly found in this area, the wind field is characterized by fairly uniform easterlies. This simple flow regime helps highlight the effect of the data on the analyzed winds.

As in Fig. 6a, Fig. 6c shows two surface wind analyses, one with (black) and one without (red) rain-flagged data. As in the previous case, the analyzed winds are reduced by up to 4 m s^{-1} (vector wind difference) in

→

FIG. 6. Surface wind analyses with GOES IR brightness temperature (K) for cases of (a), (b) synoptic front 1415 UTC 16 Oct 1996, and (c), (d) tropical convection 1415 UTC 27 Oct 1996. (a), (c) Two wind analyses are plotted in each: 1) rain-flagged data included in analysis (black) and 2) rain-flagged data excluded from analysis (red). Full wind barbs are 10 kt. The vector wind speed difference between black and red analyses is contoured every 1 m s^{-1}. NSCAT wind vector cells flagged for rain rate >5 mm h^{-1} are denoted by blue bull's-eyes. (b), (d) Close-up of 50-km scatterometer wind ambiguities near rain-flagged points in (a), (c). (a) An inset from Fig. 5.

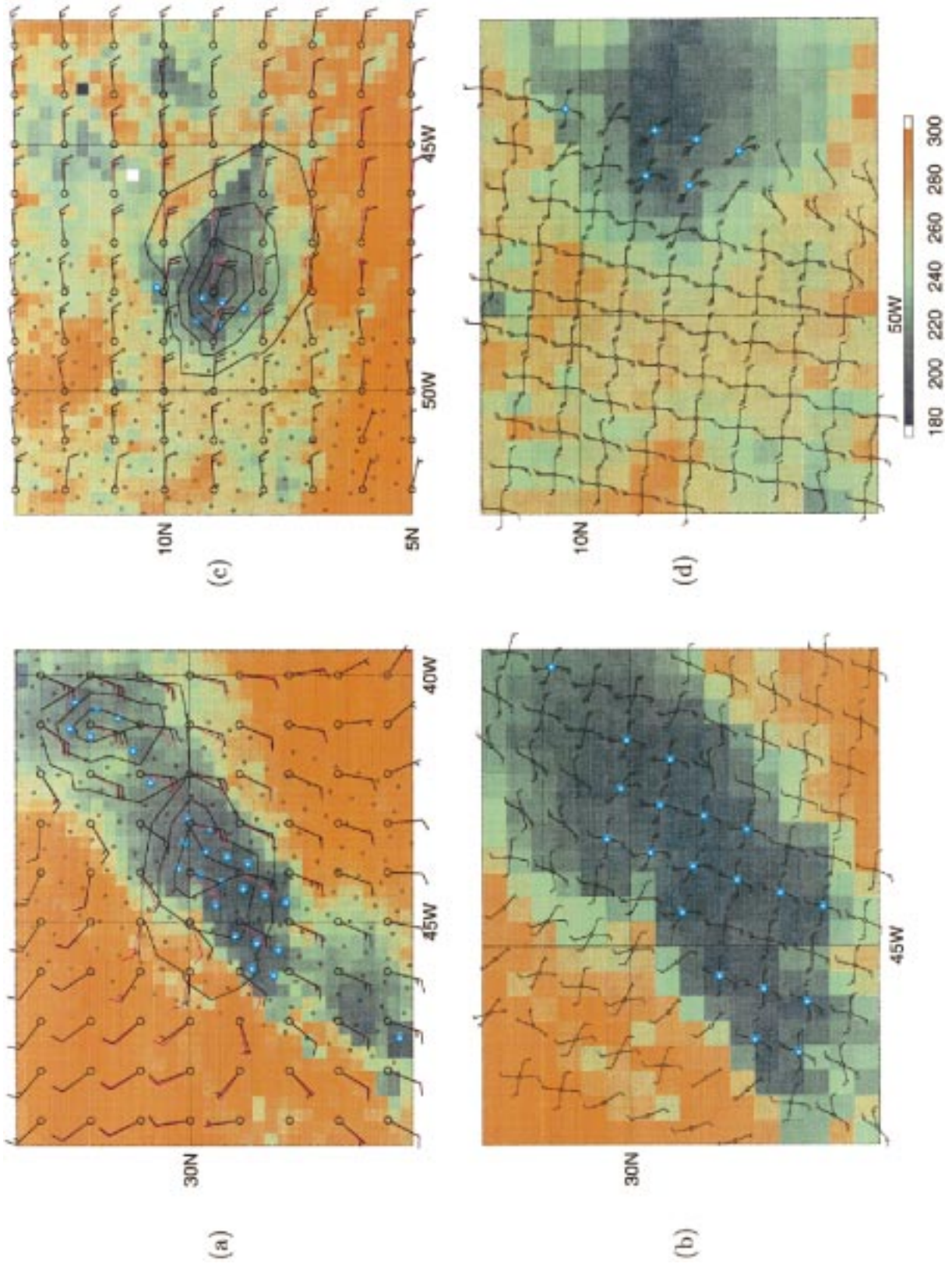

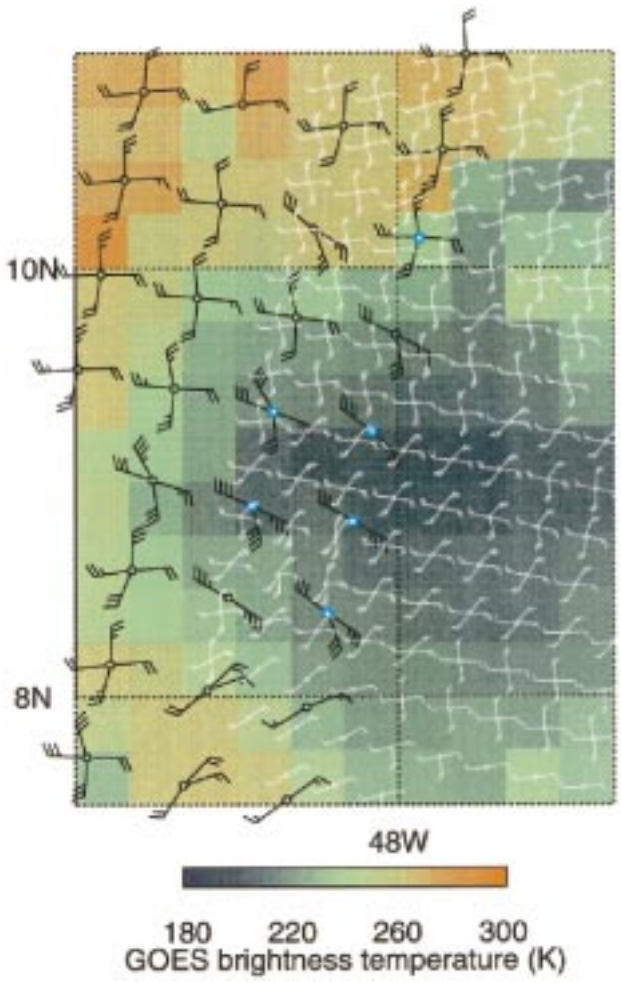

FIG. 7. Collocated *ERS-2* and NSCAT data for the case of tropical convection shown in Fig. 6d. *ERS-2* wind ambiguities (white barbs) valid 1325 UTC 27 Oct 1996, and NSCAT ambiguities (black barbs) valid 1424 UTC are both plotted on collocated *GOES-8* IR data valid 1345 UTC. NSCAT wind vector cells flagged for rain rate >5 mm h^{-1} are denoted by blue bull's-eyes. Note the large differences in *ERS-2* and NSCAT wind speeds for the coldest IR temperatures.

the vicinity of excluded data. Elsewhere, the surface winds are unchanged. The scatterometer winds where rain is suspected stand in contrast to surrounding scatterometer observations and the background wind field (see Fig. 6d). Observed wind speeds are $\sim$5 m s^{-1} greater and the wind direction of the ambiguities closest to the presumed easterlies is from the southeast. As expected, when these data are included in the analysis, the analyzed wind speed increases and a southerly component is introduced.

Further information related to these measurements is provided in Fig. 7, which contains collocated data from the European Space Agency *European Remote Sensing Satellite-2* (*ERS-2*) scatterometer, version 3, processed by Institut Français de Recherche pour l'Exploitation de la Mer (IFRE MER/CERSAT), which was available at nearly the same time (valid at 1325 UTC, approximately 1 h earlier than NSCAT). The *ERS-2* scatterometer operates at the C band (5.3 GHz), and is therefore only minimally affected by precipitation. We see that outside the areas of coldest IR cloud-top temperatures the NSCAT ambiguities (black barbs), and the *ERS-2* ambiguities (white barbs) are in very good agreement, with the most likely winds coming from the east or northeast at 10–20 kt. However, in the area of locally anomalous NSCAT winds, where wind direction changes to the southeast, and speed clearly increases to between 30 and 40 kt, we see no corresponding speed anomalies in the *ERS-2* winds, which remain at approximately 15–25 kt. This feature is consistent with the idea that increased direct backscatter from raindrops within the NSCAT scatterometer beam has resulted in spuriously high retrieved wind speeds. Since the incidence angle (and thus the amount of liquid water in the path) varies with antenna, it is also possible that the retrieved wind direction may be affected. Thus in this case, it it would be correct to flag these observations as rain contaminated.

c. Discussion

In both cases shown here, when we remove from the analysis the NSCAT data points that are suspected of contamination by heavy rain, the effect is to reduce the analyzed wind speed. Without independent data, the accuracy of one analysis compared to another cannot be determined. But the explanation for the scatterometer wind speeds and directions in potentially raining areas is somewhat uncertain; excluding the flagged data only removes a small fraction of the available data and still produces a reasonable analysis.

The relatively high scatterometer wind speeds can be viewed as 1) a feature in the true wind field, 2) an artifact of the scatterometer measurements, or 3) a combination of effects. From a meteorological perspective, increased surface wind speeds could simply be the result of a downward flux of momentum. Higher wind speeds are often observed in the vicinity of well-developed fronts or convective areas. From this perspective, the observations are a reflection of the true winds and are therefore valuable information. In this instance, one would want to retain these observations since they reflect the true state of the surface wind field. On the other hand, the observation of increased surface wind speeds may result from rainfall contamination. For example, we expect rain to roughen the sea surface when the winds are light, and a roughened sea state increases backscatter at oblique incidence angles, which ultimately increases the retrieved wind speed. At high wind speeds (>15 m s^{-1}), rain can dampen the surface capillary and short gravity waves reducing the measured backscatter, which decreases the retrieved wind speed. Additionally, direct backscatter (attenuation) from rain droplets within the scatterometer beam can also increase (decrease) measured backscatter. These are all effects due to rain and

have no relation to the actual wind. It is not clear the extent to which each of these effects is present in the cases examined. In at least one case shown here, the fortuitous availability of collocated *ERS-2* scatterometer data implies that the NSCAT winds are higher due to increased direct backscatter. Recent work reported by Smith and Wentz (1998) supports the notion that some or all of these effects are present depending on the magnitude of the true wind speed.

The analysis method is such that excluding data points will give more weight to the background field in those areas. Clearly, if the background field is wrong (a distinct possibility over the tropical oceans), removing the data that is suspected of rain contamination may not improve the analysis. More work is needed to determine whether the expected rain contamination error is larger than the expected background error.

4. Conclusions and further work

We have used rain rates derived from SSM/I data to estimate the optimal albedo and blackbody temperature thresholds for a given rain rate. Even though this thresholding method is relatively poor at predicting the instantaneous rain rate, with Heidke skill scores no better than about 0.5, it does detect the heaviest rainfall rates successfully. It is therefore useful as a simple way to flag data points that may be contaminated by heavy rain, especially when false alarms are not too important. The difference in the optimal thresholds between the Tropics and the higher latitudes is not very large. The variation with time appears larger, but is probably the result of a sampling problem due to the small number of points with heavy rain during some of the studied periods. The results of the threshold method that were presented here are somewhat preliminary. We have focused only on one area of the globe and one season. More work is required before it can be stated with confidence that a single set of thresholds is sufficient for all cases.

The intrinsic limitations of the two-channel approach suggest room for improvement. Recent work by Velden and Olander (1998) using differences between GOES 6.7- and 11-μm brightness temperatures to detect deep convection associated with tropical cyclones may prove fruitful, and would also have the advantage of being applicable during both daytime and nighttime. A number of other ways to flag NSCAT data may also be feasible. For example, the DMSP *F-10* satellite orbit closely followed that of ADEOS for about 40% of the NSCAT data; in these cases a flag based directly on SSM/I is possible. Also, since intense precipitation often has significant small-scale variability, the horizontal consistency of the backscatter measurements themselves could be used to develop another quality flag, which presumably would be related to rain. Perhaps ultimately several flags would be combined.

Using the optimal thresholds for albedo and blackbody temperature, we flagged and eliminated NSCAT data suspected of rain contamination from a series of surface wind analyses. The number of rain-flagged wind vector cells in each analysis is small and localized. The impact of excluding the rain-contaminated winds is generally <5 m s^{-1} and localized ($<5°$ of latitude and longitude). In some cases, the effect of excluding just one to five raining points can change the resulting analysis significantly, because their placement is critical for defining the flow along a front or some other shear-dominated environment.

Because of a lack of independent wind data we cannot say, at this stage, whether eliminating flagged data from the NSCAT wind analyses is always beneficial. It depends, at least in part, on the analysis method and the accuracy of the background field used in the analysis. More work is needed in evaluating the magnitude of the expected error due to rain contamination, and comparing it to the expected background field error. Further comparison of the analyses with independent in situ wind data from ships or buoys, or with collocated satellite observations such as the *ERS-2* scatterometer would be most valuable. For NWP applications, the impact on forecast skill is the most critical aspect. Impact studies in an NWP setting using the scatterometer data and several rain-flagging schemes should be conducted.

Acknowledgments. This work was supported under NASA Contracts NAS5-918 and NAS7-1260.

The NSCAT data were obtained from the NASA Physical Oceanography Distributed Active Archive Center at the Jet Propulsion Laboratory/California Institute of Technology. We also thank Frank Wentz and Remote Sensing Systems, Inc., for providing the gridded SSM/I rain-rate data. IFREMER and ESA supplied the *ERS-2* data.

REFERENCES

Arkin, P. A., 1979: The relationship between fractional coverage of high cloud and rainfall accumulations during GATE over the B-scale array. *Mon. Wea. Rev.*, **107,** 1382–1387.

Barrett, E. C., and D. W. Martin, 1981: *The Use of Satellite Data in Rainfall Monitoring.* Academic Press, 340 pp.

Doswell, C. A., III, R. Davies-Jones, and D. L. Keller, 1990: On summary measures of skill in rare event forecasting based on contingency tables. *Wea. Forecasting,* **5,** 576–585.

Ebert, E. E., 1995: Results of the Third Algorithm Intercomparison Project (AIP-3) of the Global Precipitation Climatology Project (GPCP). Bureau of Meteorology Research Centre, Melbourne, Australia. [Available from BMRC, GPO Box 1289K, Melbourne 3001, Australia.]

Grassotti, C., and L. Garand, 1994: Classification-based rainfall estimation using satellite data and numerical forecast model fields. *J. Appl. Meteor.,* **33,** 159–178.

Guymer, T. H., J. A. Businger, W. L. Jones, and R. H. Stewart, 1981: Anomalous wind estimates from the Seasat scatterometer. *Nature,* **294,** 735–737.

Hoffman, R. N., 1984: SASS wind ambiguity removal by direct minimization. Part II: Use of smoothness and dynamical constraints. *Mon. Wea. Rev.,* **112,** 1829–1852.

Negri, A. J., and R. F. Adler, 1987: Infrared and visible satellite rain

estimation. Part I: Grid cell approach. *J. Climate Appl. Meteor.*, **26,** 1553–1564.

Smith, D. K., and F. J. Wentz, 1998: NSCAT wind retrieval within high rain events. *Extended Abstracts, American Geophysical Union Spring Meeting,* Boston, MA, Amer. Geophys. Union. [Available online at http://www.agu.org.]

Smith, E., and Coauthors, 1998: Results of WetNet PIP-2 project. *J. Atmos. Sci.,* **55,** 1483–1536.

Spencer, M., and M. Shimada, 1991: Effect of rain on Ku-band scatterometer wind measurements. *Proc. Int. Geoscience and Remote Sensing Symp.* (*IGARSS '91*), Espoo, Finland, IEEE, 1285–1288.

Velden, C. S., and T. L. Olander, 1998: Bispectral satellite technique for delineating intense convection: Applications to tropical cyclones. Preprints, *Ninth Conf. on Satellite Meteorology and Oceanography,* Vol. 2, Paris, France, Amer. Meteor. Soc. 458–461.

Wentz, F. J., 1992: Measurement of oceanic wind vector using satellite microwave radiometers. *IEEE Trans. Geosci. Remote Sens.,* **30,** 960–972.